

technology can be considered commercially viable, such as the low operating temperature currently used,¹¹ which will require further efforts in the development of high-temperature storage materials.

REFERENCES AND NOTES

1. D. Psaltis and F. Mok, *Sci. Am.* **273**, 70 (November 1995).
2. J. F. Heanue, M. C. Bashaw, L. Hesselink, *Science* **265**, 749 (1994).
3. M. P. Bernal *et al.*, *MRS Bull.* **21**, 51 (1996).
4. E. S. Maniloff *et al.*, *Appl. Opt.* **34**, 4140 (1995).
5. T. W. Mossberg, *Opt. Lett.* **7**, 77 (1982).
6. X. A. Shen, E. Chiang, R. Kachru, *ibid.* **19**, 1246 (1994).
7. T. Mossberg, R. Kachru, S. R. Hartmann, A. Flusberg, *Phys. Rev. A* **20**, 1976 (1979); V. V. Samartsev, R. G. Usmanov, G. M. Ershov, B. Sh. Khamidullin, *Sov. Phys. JETP* **47**, 1030 (1978); V. A. Zuikov, V. V. Samartsev, R. G. Usmanov, *JETP Lett.* **32**, 270 (1980); J. B. W. Morsink, W. H. Hesselink, D. A. Wiersma, *Chem. Phys. Lett.* **64**, 1 (1979).
8. The fundamental difference between the present technique and the persistent spectral hole-burning (PSHB) holographic recording [see, for example, A. Renn *et al.*, *J. Lumin.* **38**, 37 (1987)] is that in PSHB, the sample is exposed simultaneously to two laser beams and a spectral hole is burned at the laser wavelength. The depth of the hole at a given spatial location varies according to the spatial interference pattern generated by both beams, and no temporal information is recorded in the holograms. These holograms are known as volume holograms, identical to those obtained in photorefractive memories. The technique also differs significantly from the accumulated photon echo (APE) memory in that APE uses multiple pairs of write and data pulses to record a single image at one spectral location [P. Saari, R. Kaarli, A. Rebane, *J. Opt. Soc. Am. B* **3**, 527 (1986)].
9. R. Yano, M. Mitsunaga, N. Uesugi, *Opt. Lett.* **16**, 1884 (1991).
10. The SLM used in the present experiment is a liquid-crystal array taken from a commercial projection television. The array consists of 480 pixels by 440 pixels and has a fill factor of ~24%. This low fill factor introduces a large insertion loss in the transmitted beam. We measured the loss for the zeroth-order transmission to be ~97% at 580 nm. We chose a 5 × 5 region of the SLM to represent a data bit and used a total of 3360 bits (60 bits by 56 bits) in each data frame to cover a center area equal to about 40% (~1.6 cm × 1.3 cm) of the SLM.
11. The length of the data pulse varied from 11.2 to 50 μs. This pulse was biphasic-modulated with pseudo-random code [Y. S. Bai and R. Kachru, *Opt. Lett.* **18**, 1189 (1993)] to reduce coherent saturation as well as echo fluctuations caused by laser wavelength instability. The write and read pulses were 10-μs-long square pulses with a peak power of only ~200 mW. These pulses were also biphasic-encoded but with the 5-bit Barker code [see, for example, M. N. Cohen, in *Principles of Modern Radar*, J. L. Eaves and E. K. Reedy, Eds. (Van Nostrand Reinhold, New York, 1987), p. 465] to increase the data channel width to ~500 kHz. Such an increase of channel width makes the memory system more tolerant to laser wavelength instability and hence reduces the fluctuation of echo intensity.
12. To achieve the required frequency precision, we used a Coherent ring dye laser and further frequency-stabilized the laser by using the Pound-Drever-Hall method [R. W. P. Drever *et al.*, *Appl. Phys. B* **31**, 97 (1983)]. By using an intracavity electro-optic modulator and locking the laser to an external reference cavity, we substantially reduced laser noise with frequencies above ~1 kHz and achieved a laser linewidth with respect to the cavity of ~40 kHz over a time period of 20 ms. We accomplished WDM by tuning the laser externally with an acousto-optic modulator to achieve a channel access time of ~1 μs.
13. For a detailed discussion on the advantages of using

WDM in frequency-selective storage materials, see, for example, B. Kohler *et al.*, *Opt. Lett.* **18**, 2144 (1993).

14. D. Psaltis, D. Brady, K. Wagner, *Appl. Opt.* **27**, 1752 (1988).
15. The intensified CCD camera has an array of 768 pixels by 484 pixels. However, the frame grabber digitizes the captured images at a reduced horizontal resolution of 640 pixels per line. The data frame from the SLM is imaged (1:1) onto the CCD array, resulting in an average bit size of 10.7 pixels × 8.4 pixels after digitization. The mismatch between the frame grabber and CCD, and that between the CCD and SLM, as well as the low spatial resolution of the intensifier (~64 line pairs per

millimeter), prevented the use of small bit dimensions. We used these mismatched devices because they were readily available and made no attempt to match their dimensions.

16. M. M. Wang *et al.*, *Opt. Lett.* **22**, 558 (1997).
17. This research was supported by the Defense Advanced Research Projects Agency (DARPA) under contract F49620-95-C-0077 and by Air Force Office of Scientific Research (AFOSR) under contract F49620-95-C-0029. Helpful suggestions and discussions with R. Leheny of DARPA and A. Craig of AFOSR are gratefully acknowledged.

27 May 1997; accepted 22 August 1997

Nanotube Nanodevice

Philip G. Collins, A. Zettl,* Hiroshi Bando, Andreas Thess, R. E. Smalley

A scanning tunneling microscope (STM) was used to explore the local electrical characteristics of single-wall carbon nanotubes. As the STM tip was moved along the length of the nanotubes, well-defined positions were found where the transport current changes abruptly from a graphitic-like response to one that is highly nonlinear and asymmetrical, including near-perfect rectification. The observations are consistent with the existence of localized, on-tube nanodevices of a type proposed theoretically.

Carbon nanotubes (1) constitute a fascinating new class of materials with a broad range of potential applications. Electronically, nanotubes are expected to behave as ideal one-dimensional (1D) "quantum wires" with either semiconducting or metallic behaviors, depending on geometrical tube parameters (2–4). The joining of dissimilar tubes could result in nonlinear junction devices formed from only a handful of carbon atoms. It has been suggested that localized defects, such as pentagon-heptagon pairs, can be the basis of nanoscale nanotube devices (5–8). We used an STM to explore the local electrical characteristics of carbon single-wall nanotubes (SWNTs). By moving the STM tip along the length of the nanotubes, we found well-defined positions where the transport current changes abruptly from a graphitic-like response to one that is highly nonlinear and asymmetrical, including near-perfect rectification. The observations are consistent with the existence of localized, on-tube nanodevices of the type that have been explored theoretically. Such device properties, when combined with the high mechanical strength (9) and anticipated

high thermal conductivity of nanotubes, point toward several future electrical, mechanical, and electromechanical applications, including those on size scales inaccessible by current lithographic methods.

The SWNTs used in this study were synthesized through a laser-assisted process described previously (10). The nanotubes were purified in oxygen at 750°C to remove undesirable amorphous and graphitic material. X-ray and electron diffraction studies on nanotubes from the same preparation batch indicated that a large proportion of the SWNTs thus produced have 1.36 nm diameters and zero chirality (so-called "armchair" tubes); the tube diameters are presumed uniform over micrometer-length scales.

Crystalline "ropes" of close-packed parallel-aligned tubes tend to form with average diameters of 20 nm. Previous fixed, large-contact electrical conductivity measurements on such nanotube ropes have shown a metallic-like behavior at room temperature and activated or localized behavior at low temperatures, as expected from quantum 1D wires (11–13).

We prepared samples suitable for STM characterization by pressing the purified SWNT material onto a gold-coated glass substrate, which left behind a thick film or mat of randomly aligned nanotubes. To eliminate extrinsic sources of damage to the SWNTs, we performed no other processing of the surface. The local electronic structure of the nanotubes was determined with a specially constructed STM with in

P. G. Collins and A. Zettl, Department of Physics, University of California at Berkeley, and Materials Sciences Division, Lawrence Berkeley National Laboratory, Berkeley, CA 94720, USA.

H. Bando, Physical Science Division, Electrotechnical Laboratory, Tsukuba, Ibaraki 305, Japan.

A. Thess and R. E. Smalley, Center for Nanoscale Science and Technology, and Departments of Chemistry and Physics, Rice University, Houston, TX 77005, USA.

*To whom correspondence should be addressed. E-mail: azettl@physics.berkeley.edu

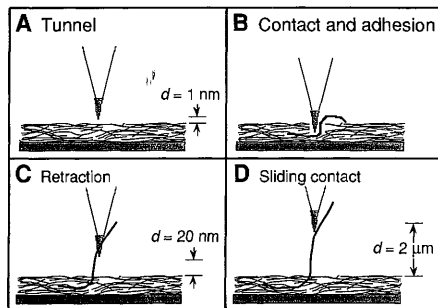


Fig. 1. Schematic of the procedure for measuring nanotube characteristics with a single STM tip.

situ current-voltage (*I-V*) spectroscopic analysis. The STM had cryogenic capability but was operated only at room temperature. It was fitted with commercially prepared platinum tips (14), which were ultrasonically cleaned just before use.

The inherent high flexibility and surface “stickiness” of high-purity SWNTs (leading to the abundant formation of “ropes” in the growth process) was exploited in our position-dependent conductivity experiments, in which the STM tip was used as a sliding local probe contact along the length of the nanotube. Figure 1 schematically depicts the STM operation sequence and probable nanotube orientation at different stages of the experiment. Unlike conventional STM operation, the STM tip was used as a 3D sample manipulator in addition to determining local electronic structure. From a position of stable tunneling (Fig. 1A), the STM tip was initially driven forward ~ 100 nm into the nanotube film (Fig. 1B). After retraction of the tip well beyond the normal tunneling range, nanotube material remained in electrical contact with the tip (Fig. 1C). This adhesion of the nanotubes to a bare metal STM tip was not observed for tubes that do not bind together into ropes, namely, multiwalled nanotubes, contaminated SWNTs, or tubes with a broader distribution of geometries. Presumably, the same van der Waals forces that so effectively bind the SWNTs together into ropes also bind the nanotubes to the STM tip, even as the tip is withdrawn from the film. At a height 200 to 300 nm above the original surface, electrical contact from the tip to the nanotube mat was maintained for $\sim 5\%$ of the samples prepared.

Conductivity measurements were begun only on nanotubes that remained electrically connected after retracting the STM tip by ~ 300 nm. With the feedback disabled, a fine stepper motor was used to further withdraw the tip from the surface in steps averaging 2 nm. Under computer control, *I-V* characteristics were obtained between each motor step until electrical contact between

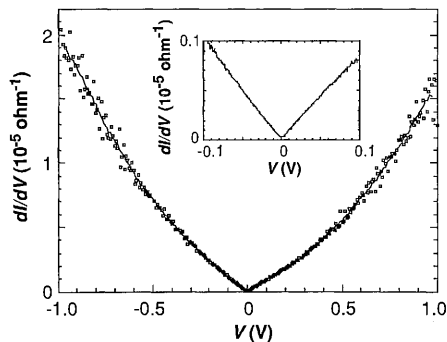


Fig. 2. Differential conductivity dI/dV of the carbon nanotubes for a contact with high conductivity; the shape near $V = 0$ is shown at higher resolution in the inset. The shape is reminiscent of dI/dV for bulk graphite.

the STM tip and the nanotube was ultimately and irreparably broken. At any given height, the mechanical movement could be interrupted to check the reproducibility of the observed *I-V* curves. For some nanotube samples, retraction of more than $2 \mu\text{m}$ occurred before electrical contact was lost, in agreement with the observed free length of the SWNTs in transmission electron microscopy (TEM) studies. Although repeating the experiment on the same exact nanotube was not possible after losing contact, further measurements on different nanotubes by the same technique showed qualitatively similar behaviors. Here, we confine our attention to measurements with no less than $1 \mu\text{m}$ of retraction, corresponding to a geometry where the nanotube unambiguously spans the distance from the mat to the STM tip.

The continuous motion of the tip allowed electrical characterization of different lengths of the nanotube material (Fig. 1D). Gradual changes were observed in the *I-V* characteristics as the STM tip was retracted, as expected from a sliding electrical contact along the surface of the nanotube. Most likely, the tip retraction cannot “unravel” the nanotube rope because of the strong intertube binding; rather, it pulls on the rope until the point of electrical contact slides. In principle, two different locations for the sliding contact are possible, one at the nanotube-to-STM tip interface, and the other at the nanotube-to-conducting mat interface. Because of the expected entanglement of the long nanotube within the mat, it is more likely that the sliding contact occurs at the nanotube-to-STM tip interface. In either case, the technique results in a position-dependent electrical transport measurement along extended lengths of selected nanotubes.

Figure 2 shows a typical normalized differential conductance (dI/dV) curve ob-

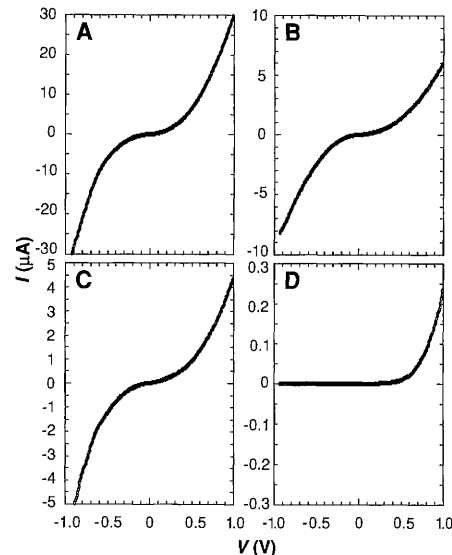


Fig. 3. Different types of current-voltage characteristics, obtained for contact points at different heights of (A) 1600, (B) 1850, (C) 1950, and (D) 1980 nm along the carbon nanotube. Note the near-ideal rectification behavior in (D).

served for extended regions along the length of the nanotube. In a conventional tunneling experiment, this plot would mimic the local density of states $N(E)$ of the material being probed. If so interpreted, the dI/dV data of Fig. 2 would suggest a local density of states with a minimum at zero bias (the Fermi energy E_F), increasing almost linearly with the magnitude of the applied bias. The dI/dV behavior closely follows the empirical form $dI/dV = A |V| (1 + bV)$. Although this expression cannot literally be taken as a density of states because of the unknown nature of our contact, it still provides a useful parameterization with typical experimental coefficients of $A = 10^{-5}$ and $b = 0.1$ for currents on the order of $I = 1 \mu\text{A}$ and biases $V \leq 1$ volt.

The response shown in Fig. 2 is not characteristic of the entire length of the nanotube. Rather, at certain extremely well-defined longitudinal positions on the nanotube surface, there occur abrupt and substantial changes in the electrical properties of the nanotube. A series of *I-V* curves were recorded at positions 1600, 1850, 1950, and 2000 nm along an SWNT rope (Fig. 3). The first three curves are nonlinear but nearly symmetric: each curve fits the empirical form described above with only gradual positional variations in the *I-V* characteristics. At a position of 2000 nm, the *I-V* characteristics abruptly changed to a marked rectifying behavior (Fig. 3D). This response (Fig. 3D) was entirely reproducible and persisted for positions up to 2300 nm, shortly beyond which electrical contact with the nanotube was broken.

Similar abrupt changes in the electronic response were observed for different nanotube specimens extracted from the mat surface. The most common response was a transition from the nearly symmetric nonlinear conductance to a highly nonlinear asymmetric conductance state involving current jumps by two to four orders of magnitude. These transitions occurred in approximately half of the samples investigated at different positions, leading to the same "device-like" curves as depicted in Fig. 3.

We argue that our position-dependent spectroscopic observations give strong evidence for the existence of localized, well-defined, on-tube "nanodevices" with response characteristics consistent with theoretical predictions. The extensive regions of linear differential conductance are depicted in Fig. 2 and Fig. 3, A to C. The conductance curves indicate that a common material density of states dominates the transport in these regions. In particular, the density of states for graphite exhibits a linear energy dependence, because the graphite E_F falls at the crossing of two electronic bands. Because SWNTs are aligned in ropes with tube-tube interactions present, a correspondence between the $N(E)$ of the rope and that of graphite might be expected, at least qualitatively. The inset to Fig. 2 emphasizes that at low bias, the nanotube differential conductivity is nearly linear. Unfortunately, difficulties in defining the nanotube-to-STM tip contact precludes any quantitative correspondence between the transport conductivity of the nanotube rope and the tunneling density of states $N(E)$ for graphite.

Because of the observation of linear differential conductivity at the low bias levels used in these experiments, it is inaccurate to speak of the linear resistivity of the nanotubes. Most transport measurements reported, however, quote resistance values for various measurement configurations. A calculation of the resistance is instructive as a comparison and to determine how many ropes span from the STM tip to the surface. Experimentally, the rope is known to span $\sim 1 \mu\text{m}$ from STM tip to the mat surface, and the ropes have diameters of 10 to 30 nm. The conductivity closest to zero bias gives a measured resistance of 100 kilohms, from which we may calculate a nanotube resistivity of $10^{-2} \text{ ohm}\cdot\text{cm}$. This resistivity is consistent with other reported values for carbon nanotubes, including SWNTs (11, 15–19), supporting the assumption that only a single rope connects the STM tip to the matted surface.

We now discuss the dramatic deviations away from this dominant behavior. The changes in conductivity occur abruptly, for incremental tip movements of only 2 nm, but are observed on different nanotubes at widely

varying distances above the substrate. Both aspects are in accord with a low-density, random distribution of nanotube defects and rule out a gradually weakening tip-tube contact as the source of the behavior. Although they could cause a similar distribution, contaminants or disconnected material between the STM tip and the nanotube rope are ruled out as a cause based on the rather substantial tip-to-tube contact interaction and the absence of extraneous nanotube wall contamination as determined from TEM observations of the purified material. Electrostatic effects were ruled out by biasing the STM tip to $\pm 4 \text{ V}$ and recording no change in the observed conductance behavior.

Other tip-related artifacts may be ruled out because of the infrequency of the dramatic changes. In particular, slippage of the tip contact point from one nanotube to another within the same rope could produce changes in the conductivity but should be as frequent as the overall twist of the nanotube bundle. Experimentally, the symmetric conductance curves vary smoothly over thousands of nanometers of tip motion, indicating that tube-to-tube slippage plays little or no role in the measured transport. Evidence for minute slippage, as well as for small changes in the contact resistance between the STM tip and the nanotubes, can be found in the small scaling variations measured throughout the experiment (Fig. 3, A to C). These variations occur on scales of tens of nanometers, as expected for the assumed sliding contact.

We argue that the extreme changes in conductivity are caused by contact with localized nanotube defects that greatly alter the local $N(E)$. Although the injected current predominantly indicates a graphitic behavior for the nanotube rope, a nanotube defect at the contact point would obscure and dominate the transport characteristic. For example, the existence of a pentagon-heptagon defect in the otherwise perfectly hexagonal nanotube wall fabric can lead to sharp discontinuities in the electronic density of states along the tube axis. It is possible to have one portion of the nanotube with metallic characteristics almost seamlessly joined to another portion that is semiconducting. The "junction" constitutes a pure-carbon Schottky barrier. This and related nanotube structures have been treated theoretically (5, 6), and they yield a rich spectrum of nanodevice characteristics, including highly nonlinear transport currents, asymmetries, and diode-like rectification. The sliding STM probe indicates exactly these types of behaviors as its position is shifted along the length of a nanotube by only a few nanometers, indicating the presence of what we identify as a localized

nanotube nanodevice.

Besides observing sharp transitions in the conductance behavior precisely at the nanodevice location, more subtle signatures of the device would be expected at distant locations. This is because the nanotube ropes are only quasi-1D conductors, whereas the highly conducting SWNTs interact with neighboring nanotubes through a relatively weak but finite interchain hopping integral. Indeed, such second-order conductance effects are observed experimentally. For example, when conductance data sets collected by sliding the STM tip over an extended region are fit to the empirical fitting function introduced above, the parameter A smoothly decreases as the tip approaches the defect location. Quasi-1D conduction is important because it helps explain why nanotube defects and nanodevices have not been detected in previous transport measurements. Lithographically defined contact pads, as are commonly used, will always contact relatively large areas on a nanotube rope, effectively shorting parallel channels together, thus providing at least one highly conducting pathway; furthermore, in nanotubes with multiple concentric walls, the isolation of a single defect-containing conducting path may not be possible, even with a local probe contact (19).

We measured distinct changes in the conductivity as the active length of the nanotube is increased, suggesting that different segments of the nanotube exhibit different electronic properties. The changes occur over very short lengths and are suggestive of on-tube nanodevices. Nanotube nanodevices could prove to be invaluable building blocks in future miniaturized electronics.

REFERENCES AND NOTES

1. S. Iijima, *Nature* **354**, 56 (1991).
2. J. W. Mintmire, B. I. Dunlap, C. T. White, *Phys. Rev. Lett.* **68**, 631 (1992).
3. N. Hamada, S. Sawada, A. Oshiyama, *ibid.*, p. 1579.
4. M. S. Dresselhaus, G. Dresselhaus, P. C. Eklund, *Science of Fullerenes and Carbon Nanotubes* (Academic Press, New York, 1996).
5. L. Chico, V. H. Crespi, L. X. Benedict, S. G. Louie, M. L. Cohen, *Phys. Rev. Lett.* **76**, 971 (1996).
6. L. Chico, L. X. Benedict, S. G. Louie, M. L. Cohen, *Phys. Rev. B* **54**, 2600 (1996).
7. R. Saito, G. Dresselhaus, M. S. Dresselhaus, *ibid.* **53**, 2044 (1996).
8. J. Charlier, T. W. Ebbesen, P. Lambin, *ibid.*, p. 11108.
9. M. M. J. Treacy, T. W. Ebbesen, J. M. Gibson, *Nature* **381**, 678 (1996).
10. T. Guo, P. Nikolaev, A. Thess, D. T. Colbert, R. E. Smalley, *Chem. Phys. Lett.* **243**, 49 (1995).
11. J. E. Fischer *et al.*, *Phys. Rev. B* **55**, R4921 (1997).
12. M. Bockrath *et al.*, *Science* **275**, 1922 (1997).
13. A. M. Rao *et al.*, *ibid.*, p. 187.
14. Obtained from Seiko Instruments, Japan.
15. L. Langer, *J. Mater. Res.* **9**, 927 (1994).
16. *et al.*, *Phys. Rev. Lett.* **76**, 479 (1996).
17. S. N. Song, X. K. Wang, R. P. H. Chang, J. B. Ketterson, *ibid.* **72**, 697 (1994).
18. A. Thess *et al.*, *Science* **273**, 483 (1996).
19. H. Dai, E. W. Wong, C. M. Lieber, *ibid.* **272**, 523 (1996).

20. We thank M. L. Cohen, S. G. Louie, and V. H. Crespi for beneficial discussions and N. G. Chopra and D. Bernaerts for performing TEM studies on our samples. Supported in part by a University of California Berkeley Chancellor's Initiative Grant (A.Z.), NSF (A.Z., R.E.S.), the U.S. Department of Energy (A.Z.), the Office of Naval Research (A.Z.), the Texas Ad-

vanced Technology Program (R.E.S.), and the Japan Agency of Industrial Science and Technology (A.Z., H.B.). P.G.C. acknowledges support from a Helmholtz Fellowship, and A.Z. received support from the Miller Institute for Basic Research in Science.

5 June 1997; accepted 4 August 1997

Neither the *ste5(C177S)* allele nor the *ste5(C177A C180A)* allele was able to complement the mating defect of an *ste5Δ* strain, when the mutant genes were expressed from a centromere-based plasmid, driven by either the *STE5* promoter or the inducible *GAL1* promoter (Table 1). Even high-level expression of the mutant proteins from the *GAL1* promoter on a multicopy plasmid caused only a small increase in the mating proficiency of the *ste5Δ* cells (Table 1). Thus, an intact RING-H2 domain is essential for Ste5 function. Consistent with this observation, *ste5Δ* cells containing the *ste5(C177A C180A)* allele were unable to activate transcription from a pheromone-inducible reporter gene (*FUS1-lacZ*) (10) in response to the mating pheromone α -factor (9). Likewise, *ste5Δ* cells expressing the *Ste5(C177A C180A)* mutant were unable to respond to α -factor (9), as judged by the halo bioassay for pheromone-induced growth arrest (11).

When *Ste5(C177A C180A)* was overexpressed from the *GAL1* promoter on a multicopy plasmid in a *STE5⁺* strain, the cells formed a halo in response to α -factor, but the halo filled in much more rapidly than did lawns of control cells lacking the plasmid (9), indicating an attenuated G_1 arrest response in these cells. Such a dominant-negative effect might result if the mutant protein competed with wild-type Ste5 for the binding of one or more of the factors required for signaling and sequestered them in an inactive complex. To determine directly whether the *Ste5(C177A C180A)* mutant protein remained competent to interact with any of the known MAPK cascade components, we immunoprecipitated extracts from cells expressing derivatives of Ste5 and *Ste5(C177A C180A)*, tagged at their NH_2 -terminal end with a c-Myc epitope, with an appropriate mono-

Ste5 RING-H2 Domain: Role in Ste4-Promoted Oligomerization for Yeast Pheromone Signaling

Carla Inouye,* Namrita Dhillon,*† Jeremy Thorner‡

Ste5 is a scaffold for the mitogen-activated protein kinase (MAPK) cascade components in a yeast pheromone response pathway. Ste5 also associates with Ste4, the β subunit of a heterotrimeric guanine nucleotide-binding protein, potentially linking receptor activation to stimulation of the MAPK cascade. A RING-H2 motif at the Ste5 amino terminus is apparently essential for function because *Ste5(C177S)* and *Ste5(C177A C180A)* mutants did not rescue the mating defect of a *ste5Δ* cell. In vitro *Ste5(C177A C180A)* bound each component of the MAPK cascade, but not Ste4. Unlike wild-type Ste5, the mutant did not appear to oligomerize; however, when fused to a heterologous dimerization domain (glutathione S-transferase), the chimeric protein restored mating in an *ste5Δ* cell and an *ste4Δ ste5Δ* double mutant. Thus, the RING-H2 domain mediates Ste4-Ste5 interaction, which is a prerequisite for Ste5-Ste5 self-association and signaling.

Mating in the yeast *Saccharomyces cerevisiae* is initiated by pheromone binding to heterotrimeric guanine nucleotide-binding protein (G protein)-coupled receptors on cells of opposite mating type, leading to dissociation of the $G\beta\gamma$ complex (Ste4 Ste18) from the inhibitory $G\alpha$ (Gpa1) subunit (1). Subsequent signal propagation activates an evolutionarily conserved MAPK cascade (2), ultimately causing arrest of the cell cycle in the G_1 phase and the production and activation of factors required for cell and nuclear fusion. Ste5 is an essential component of this pathway (3, 4) and is thought to function as a scaffold for the MAPK cascade components (5). Ste5 also associates with Ste4 (6) and thus may link release of $G\beta\gamma$ to activation of the MAPK cascade.

The NH_2 -terminus of Ste5 (residues 177 to 229) contains a cysteine-rich region that is the prototype for the RING-H2 motif (Fig. 1A). The RING-H2 motif is a variant of the larger class of RING domains (7) but contains a second histidine in place of the cysteine normally found at position 5 (Fig. 1B). Proteins possessing RING and RING-H2 domains

participate in diverse cellular processes, but no specific function has yet been ascribed to these domains (7). The crystal structures of two RING domains have been solved (8), and each is a globular pseudosymmetric fold that coordinates two Zn^{2+} atoms through a cross-bridging element. To disrupt this structure as a means to determine its importance to the function of Ste5, we mutated [to serine (S) or alanine (A), as indicated] either the first, or both the first and second, conserved cysteine (C), yielding *Cys¹⁷⁷ → Ser¹⁷⁷* (*C177S*) and *C177A C180A* mutant proteins. The expressed amount and stability of both mutant proteins were comparable to those of wild-type Ste5 (9).

A Protein	Organism	RING-H2 Domain Sequence
		177 229
Ste5	Yeast	C TLCDEPTISNRRKGEKIIELAC G HL S HQ E CLIIISFGTTSKADVRLFPF P CT R K
Deltex	<i>Drosophila</i>	C PM C MEELVHSAQNPALSL S RC Q HL M HL Q CLNGMILIAQQ N EM N KL F IE C PV C
Far1	Yeast	C LICEESISSTFTG E KV V EST C S H T S HY N CY L ML F ET L Y F Q G K F PE C K I C
Rapsyn	Human	C AL C GE S IG E K NS R L Q AL P CS H IF H LR C L Q N N G R TS C P N C
Neurodap1	Rat	C P I CC S E Y I K DD I ATE L P C H H PF H K F CV S I W L Q K S G T CP V C
Pep3	Yeast	C DE C G K FL Q IK K F I VF P CG H CF H W N C I IR V L N S N D Y (24) I VE K CG L C
Pep5	Yeast	C FM C RL T L D IP V VF K CG H I Y H Q CL N EE D TL E SE R RL F K C PK C

B Consensus **-Cys-X₂-Cys-X₁₂₋₁₇-Cys-X-His-X₂-His-X₂-Cys-X₈₋₃₉-Cys-X₂-Cys-**

Fig. 1. Sequence alignment and derived consensus for the RING-H2 motif. (A) Shown are RING-H2 domains of the following proteins (with the indicated GenBank accession numbers): Ste5 (L23856); Deltex (U09789); Far1 (M60071); Rapsyn (Z33905); Neurodap1 (D32249); Pep3 (M65244); and Pep5 (X54466). Conserved residues are indicated in bold and represent presumptive Zn^{2+} -binding ligands. (B) Consensus sequence for the RING-H2 motif. Positions conserved in all members are given in bold. X represents any amino acid, and the number of such residues is also indicated.

Department of Molecular and Cell Biology, Division of Biochemistry and Molecular Biology, University of California, Berkeley, CA 94720-3202, USA.

*These authors contributed equally to this paper.
†Present address: Laboratory of Molecular Embryology, National Institute of Child Health and Human Development, National Institutes of Health, Building 18T, Room 106, Bethesda, MD 20892-5431, USA.
‡To whom correspondence should be addressed. E-mail: jthorner@mendel.berkeley.edu